SUPPORTING INFORMATION

Collective Plasmonic Properties in Few-Layer Gold Nanorod Supercrystals

Cyrille Hamon,[a,§] *Sergey M. Novikov,*[a,b,§] *Leonardo Scarabelli,*[a] *Diego M. Solís,*[c] *Thomas Altantzis,*[d] *Sara Bals,*[d] *José M. Taboada,*[e] *F. Obelleiro*[c] *and Luis M. Liz-Marzán*[a,f,*]

[a] Bionanoplasmonics Laboratory, CIC biomaGUNE, Paseo de Miramón 182, 20009 Donostia - San Sebastián, Spain

[b] Present address: Department of Technology and Innovation, University of Southern Denmark, Odense M, DK-5230 Denmark

[c] Dept. Teoría de la Señal y Comunicaciones, University of Vigo, 36301 Vigo, Spain

[d] EMAT-University of Antwerp, Groenenborgerlaan 171, B-2020 Antwerp, Belgium

[e] Dept. Tec. Computadoras y Comunicaciones, University of Extremadura, 10003 Cáceres, Spain

[f] Ikerbasque, Basque Foundation for Science, 48013 Bilbao, Spain

Methods

Gold nanorods (GNRs) were characterized by transmission electron microscopy (TEM, JEOL 2010, 120 keV). Argon plasma cleaning process was performed in an Aja magnetron sputtering system (ATC 2200). SEM images were obtained in an ESEM Quanta250 FEG (FEI, The Netherlands). Raman scattering measurements were performed in a confocal scanning Raman microscope (micro-Renishaw InVia Reflex system equipped with Peltier-cooled charge-coupled device (CCD) detectors). The configuration involved a 1200 lines/mm diffraction grating, a 100×

objective (N.A.=0.85) and excitation wavelengths of 633 nm. SERS images (4×4 μm) were recorded by mapping the spatial dependence of SERS intensity integrated at the main Raman peaks within the shift range 1570-1650 cm^{-1}, for each of the 15×15 points in the scan with P~0.01 mW and integration time 0.5 s. These scanning parameters were selected as a compromise to obtain a significant signal from CV without bleaching. AFM mapping was performed with a Bruker NanoScope V - MultiMode system in contact mode using Brucker DNP-S10 cantilever (0.350 N/m). HAADF-STEM images and STEM-EELS maps were acquired using a monochromated double aberration corrected cubed FEI-Titan 50-80 electron microscope, operated at 300kV and electron tomography series were acquired using an aberration corrected cubed FEI-Titan 60-300 electron microscope, operated at 300kV. For the EELS data, a zero loss peak was acquired in vacuum with minimum noise in order to be fitted and subtracted from the EELS spectra acquired from the assemblies. The EELS data treatment was performed in EELSmodel.[1, 2] For electron tomography, tilt series of HAADF-STEM images were acquired from -64° to +74° with an tilt increment of 2°, by using a Fischione model 2020 single tilt tomography holder. The alignment of the series was performed by a combination of an automated and manual alignment by using the FEI Inspect3D software and IMOD, respectively.[3] The reconstruction was performed by using the Simultaneous Iterative Reconstruction Technique (SIRT) as implemented in the ASTRA toolbox using 150 iterations.[4, 5] The reconstructed volume was visualized using the Amira 3D software. All chemicals for GNR synthesis and functionalization were purchased from Sigma Aldricht.

Nanorods preparation and ligand exchange

Nanorods were obtained addition following protocols described in previous work.[6] GNR concentration was expressed as Au molar concentration, calculated from the absorbance at 400

nm.[1] For MUDOL grafting, 5 mL of freshly made GNR solution was purified by centrifugation (7000 rpm, 40 min, 29 °C) and dispersed in water to reach final surfactant and GNR concentrations of 0.75 mM and 0.3 mM, respectively. In a typical experiment, 50 μL of 10 mM MUDOL solution was mixed with the purified GNR dispersion, shaken vigorously, and incubated under mild stirring for 24 h. The obtained MUDOL GNRs were stable for months, and Au concentration was tuned between 3 and 15 mM by centrifugation (7000 rpm, 40 min, 29 °C).

Supercrystals preparation and characterization

In a typical experiment, 10 μL of GNRs were drop casted on a glass substrate (Menzel-Gläzer, Thermo Scientific) and dried in an homemade apparatus system[7] to slow down the evaporation rate up to twelve hours. Supercrystals were cleaned by Argon plasma (4W, 24 mbar Ar, 30 min) to remove organics that could interfere with Raman measurements. Crystal Violet (10 μL, 10^{-6} M in ethanol) was drop casted and dried under air.

Details on modeling

A full-wave boundary-element-based method of moments (MoM) formulation for piecewise-homogeneous penetrable objects is used to solve Maxwell's equations.[8] As opposed to point-matching techniques, MoM enforces the boundary conditions in a variational sense over the whole boundary with the help of functionals. In this regard, Galerkin's testing procedure is adopted, meaning the testing functionals are the very same basis functions used to expand the unknown electric and magnetic surface equivalent currents, div-conforming Rao-Wilton-Glisson (RWG)[9] basis functions in our case. The discretization of the set of boundary equations derived from the Stratton-Chu surface integro-differential formulas results in a non-sparse NxN matrix system of linear equations, being N=2M the number of unknowns and M the number of boundary mesh elements.

A major drawback inherent to MoM approaches is the rigorous evaluation of integrals including singular and hypersingular integrands stemming from the boundary element methods' (BEM) kernel, the three-dimensional (3D) electrodynamic homogeneous Green's function, and its derivatives. The accurate evaluation of these terms, which in the developed code are handled via subtraction and analytical evaluation, is of foremost importance and will determine the accuracy of the method. This is in contrast to volumetric field-based formulations—finite-difference time-domain (FDTD) technique, finite-elements methods (FEM), e.g.—, usually free of such singularities. In return, nevertheless, MoM provides a key advantage in nanoplasmonics: as the field singularities and hotspots arising with localized surface-plasmon resonances (LSPRs) are analytically addressed, the method does not suffer from numerical dispersion or instability due to rapid field variations, as may be the case with volumetric solvers.

In addition, despite BEM reducing the problem's number of degrees of freedom if compared with the 3D parameterization involved in volumetric approaches, and hence rendering the problem more viable in terms of computational resources, a means to compress the rank-deficient MoM impedance matrix that expedites the $O(N^2)$ matrix-vector product (MVP) in the framework of an iterative solver is still paramount. Among the various algebraic or physics-based electrodynamic compression techniques found in the literature, the fast multipole method (FMM)[10] and its multilevel version (MLFMA)[11] are arguably the most successful, the latter achieving an impressive and error-controllable $O(N\log N)$ computational cost. The key to this high compression rate relies upon a decomposition of the Green's function in spherical harmonics and further plane-wave expansion. This allows for a factorization of the Green's function-based MoM cross-couplings through the Gegenbauer addition theorem, in virtue of which the non-nearest neighbor interactions can rather be grouped in communication "hubs", thus avoiding the N^2 all-

to-all communication scheme present in uncompressed MoM. This grouping can be straightforwardly performed in a hierarchical multilevel fashion with an oct-tree decomposition of the geometry following a Cartesian grid. In doing so, the radiating/receiving centers of the groups lie on a regular 3D lattice and thus the translation operator among groups for a given direction in the plane-wave k-space can be seen as a circular 3D convolution. Consequently, it can be simultaneously sped up for all groups as a product in the transformed space through the use of a 3D fast Fourier transform (FFT). Such implementation has proved to solve large-scale plasmonic problems in an accurate and efficient way.[12, 13]

One step forward in the full-wave analysis of electrically-large assemblies consisting of a reduced set of plasmonic nanoparticles highly repeated throughout the structure, consists of the hybridization of both MoM and MLFMA,[14] which exploits the repetition pattern inherent to this kind of nanostructures. Loosely put, the repeated self-coupling naturally-split problems are squarely solved throughout the factorization of their MoM impedance matrix blocks (dense, though small), enabling the Krylov-space iterative method—generalized minimal residual method (GMRES)—to focus solely on the cross-couplings through the surrounding medium, spectrally comptacted with MLFMA. This is done with the inclusion of a Jacobi diagonal block preconditioner which, through the lower-upper (LU) decomposition of the repeated self-impedance submatrices and subsequent forward- backward substitutions, dramatically reduces the iteration count needed to reach a given residual error, strongly enhancing the convergence behavior of the electromagnetic solver.

When dealing with large densely-packed arrangements as the pieces of plasmonic metamaterial at hand, however, the geometrical features lead to such overly-populated meshes that the non-compressed interactions between nearest-neighbors in MLFMA yield the problem unfeasible,

unless supercomputers are used. The origin of this limitation can be traced back to the plane-wave expansion of the Green's function, wherein the spherical Hankel function of the second kind present in the translation stage becomes unstable for small arguments, i. e., for low-frequency problems ruled by circuit-like evanescent wave physics rather than propagation physics. This is known as "sub-wavelength breakdown" and translates, in practice, into a geometry partition with a cellsize that should not go below $\sim \lambda/10$ at the finer level, being λ the wavelength in the background medium.

The present work exploits the repetition pattern found in metamaterials in order to compress these rank-deficient neighbor couplings in the finer level of the MLFMA decomposition, governed by quasi-electrostatic physics, through truncated singular value decompositions (SVD)[15] that compensate their high computational demand, in relative terms with respect to the block size, with the fact that those coupling blocks are periodically repeated throughout the structure. If we consider the $2L$x$2L$ coupling block that defines the interaction between a pair of close strongly coupled nanorods, each discretized with L=1656 RWG's, its rank r for a prescribed threshold ϵ (ϵ=1e^{-3} has proved to be a judicious value) is found to be typically below L/10, and thereby the effective number of degrees of freedom (DoF) can be fitted if the SVD factorization is truncated including only the first r singular values (σ), provided that $\sigma_{r+1} < \epsilon\sigma_1$. If, in contrast to the more conventional Cartesian grid, the multilevel decomposition is defined in terms of growing sets of entire nanoparticles (nanorods in this case) that are periodically repeated, this compact representation for the coupling interactions among cells can be recycled. The memory footprint achieved with this approach for the four-layer case is in the order of only ~2 GB if $\epsilon = 10^{-3}$ is chosen for truncation and ~20 GB without truncation. Otherwise, more than

300 TB would be needed for conventional MLFMA with a Cartesian oct-tree starting at $\lambda/10$, rendering the analysis nonviable.

The authors would like to stress out that the developed methodology is a rigorous full-wave approach. Consequently, the scattering response does take into account all interactions, including edge effects, as infinite-structure considerations have been ruled out. The dispersive electric permittivity for Au was taken from ref.[16]

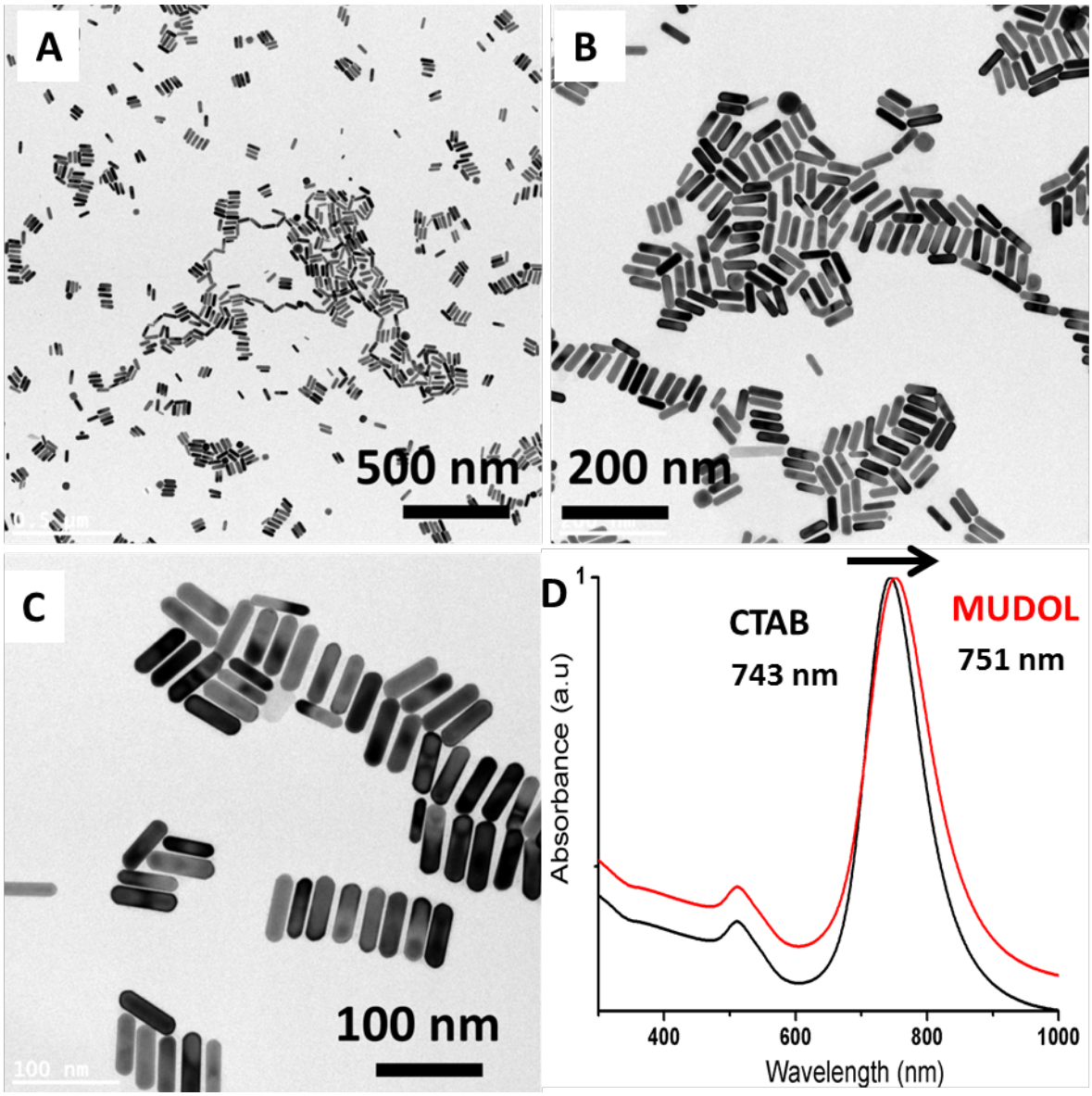

Figure S1. TEM characterization of Au nanorods. **A-C)** Representative TEM images of as synthesized nanorods with a mean length of 55±6 nm, a mean width of 17±2 nm and an aspect ratio of 3.2, at different magnification. Statistics were performed over 100 particles. **D)** UV- Vis spectra of GNR colloids before (black) and after (red) replacing CTAB with MUDOL. A slight shift of the longitudinal plasmon band from 743 nm to 751 nm was measured.

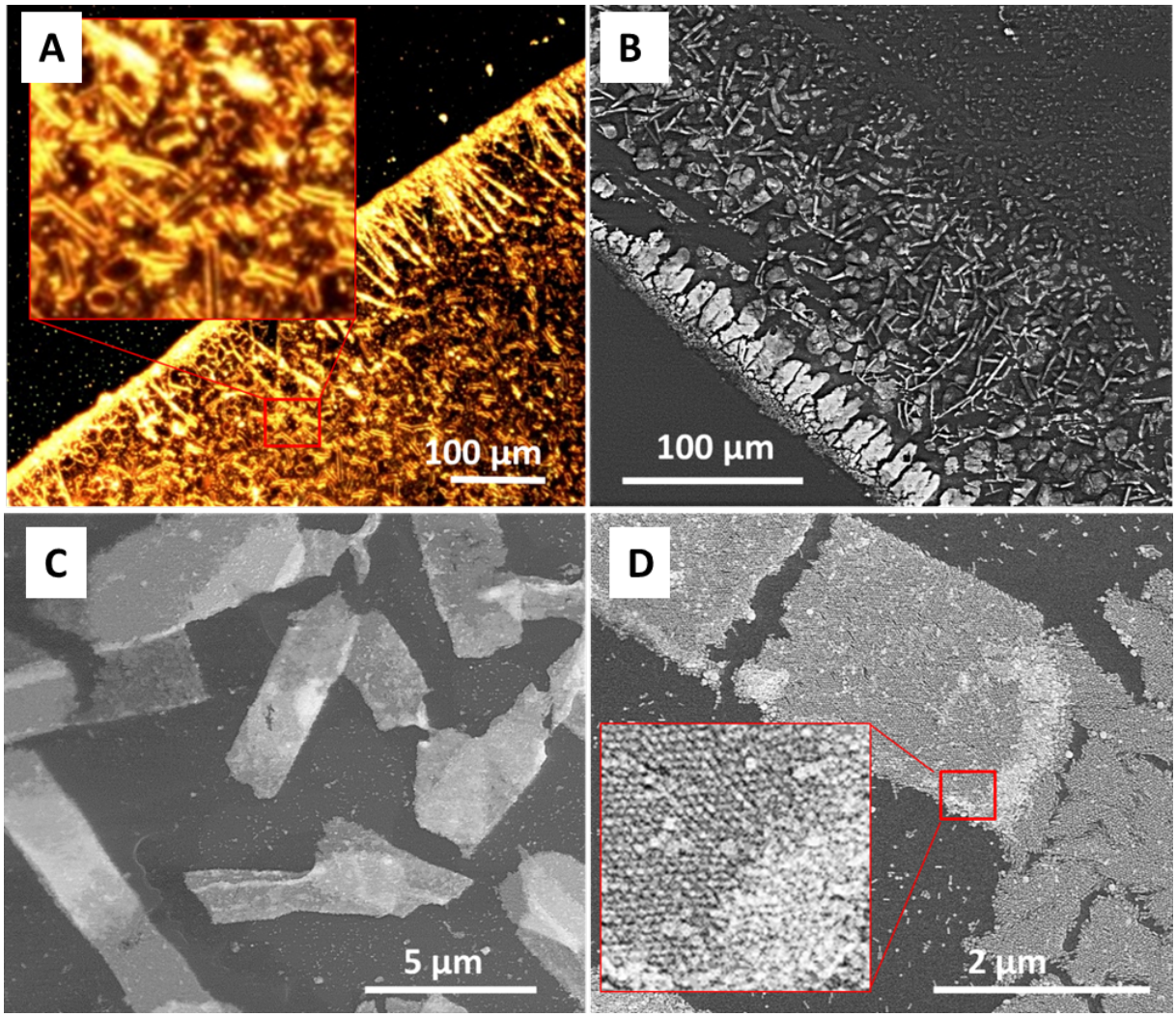

Figure S2. Characterization of CTAB-GNR supercrystals. **A)** Dark Field image acquired from the region of the coffee ring. **B-D)** Representative SEM images of CTAB-GNR supercrystals at different magnifications. CTAB concentration was 2.5 mM and Au^0 concentration before drop casting was 3 mM.

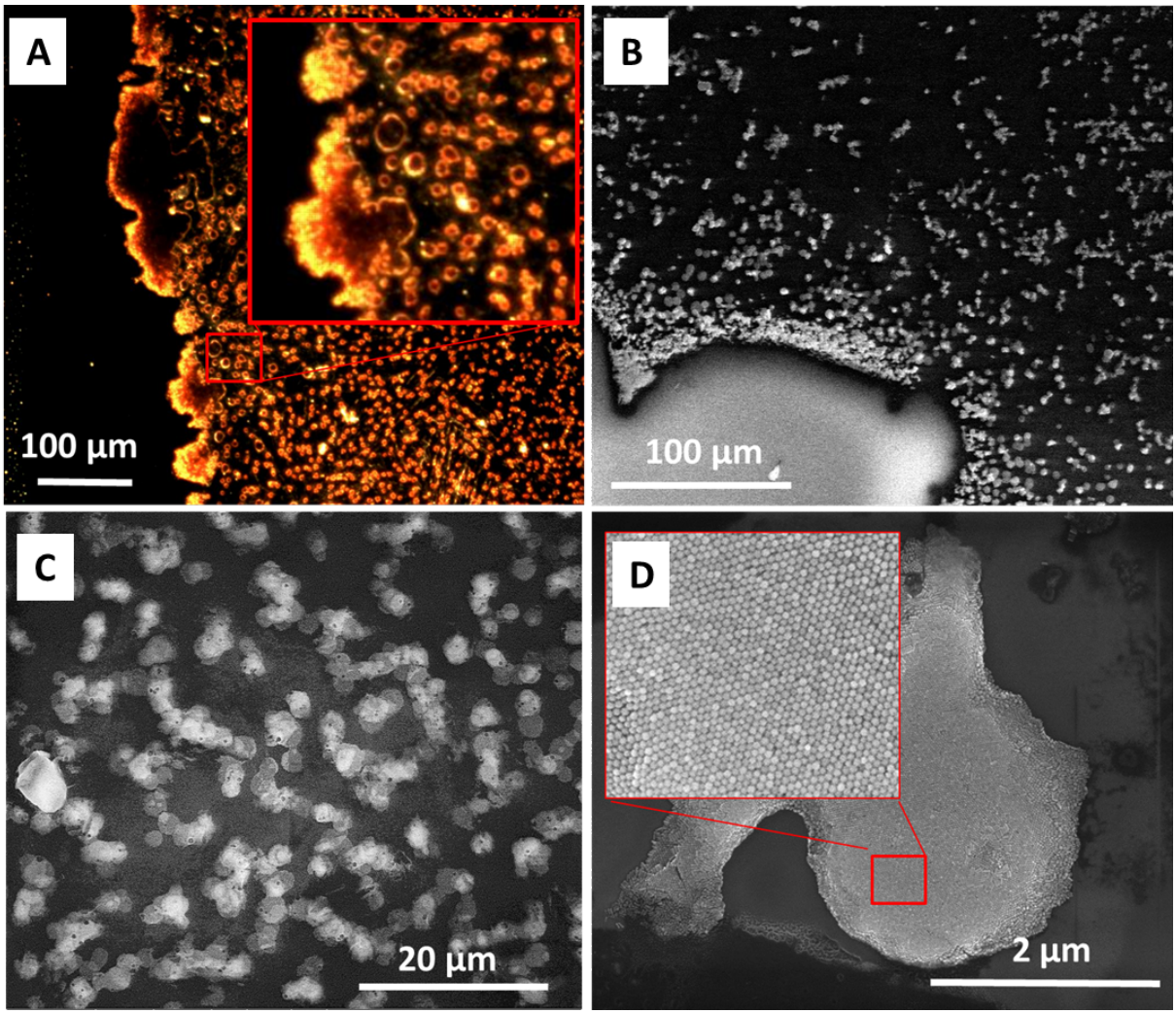

Figure S3. Characterization of MUDOL-GNR supercrystals. **A)** Dark field optical micrograph acquired from the region of the coffee ring. **B-D)** Representative SEM images of MUDOL-GNR supercrystals at different magnifications. CTAB and MUDOL concentrations were below the CMC and at 0.1 mM, respectively. Au^0 concentration before drop casting was 3 mM.

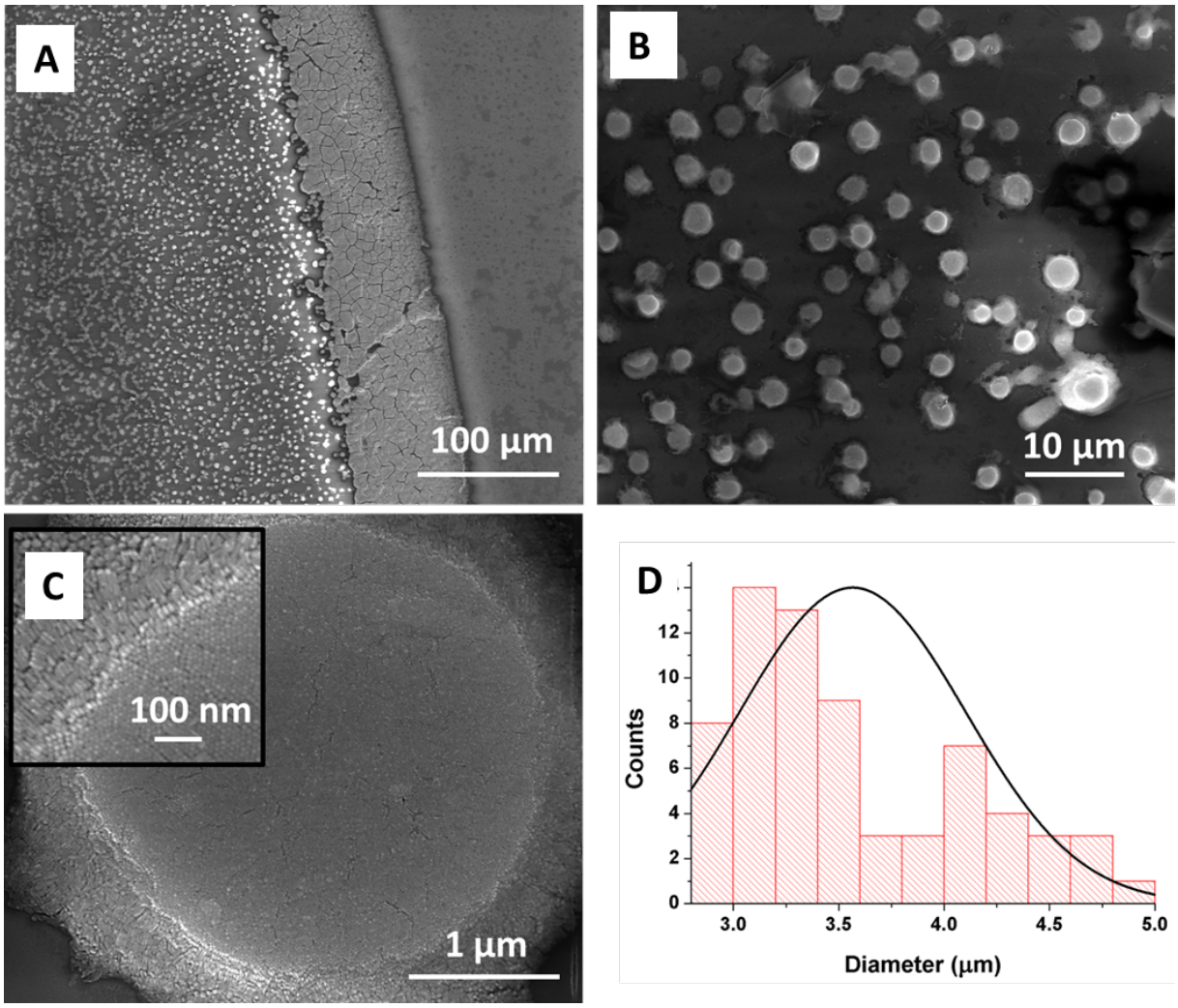

Figure S4. Characterization of MUDOL-GNR supercrystals with an Au^0 concentration before drop casting of 15 mM. **A-C)** Representative SEM images of MUDOL-GNR supercrystals at different magnifications. **D)** Histogram of supercrystal diameters showing an average diameter of 3.58 µm. CTAB and MUDOL concentrations were below CMC and 0.1 mM, respectively.

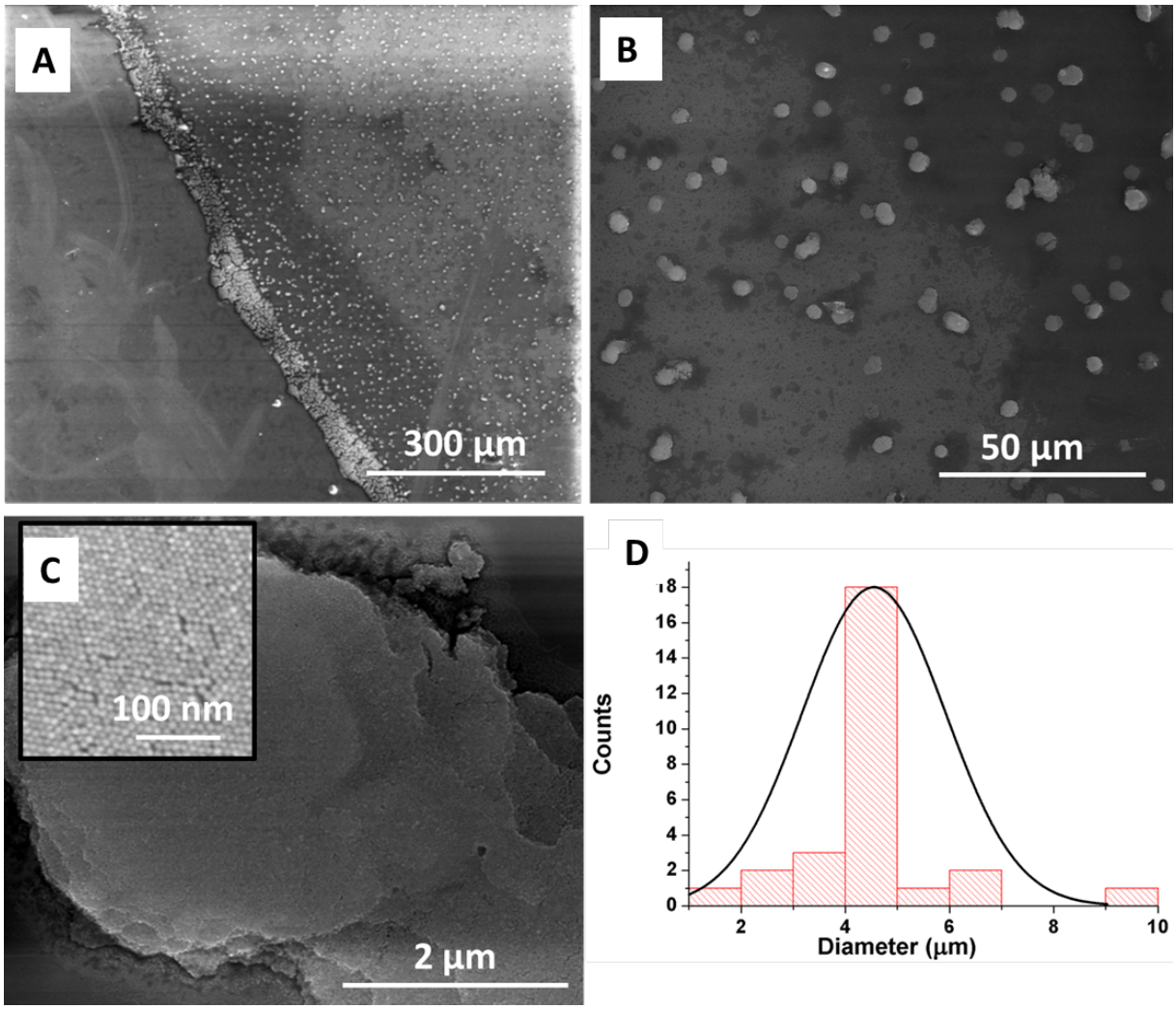

Figure S5. Characterization of MUDOL-GNR supercrystals with an Au^0 concentration before drop casting of 3 mM. **A-C)** Representative SEM images of MUDOL-GNR supercrystals at different magnifications. **D)** Histogram of supercrystal diameters showing an average diameter of 4.51 µm. CTAB and MUDOL concentrations were below CMC and 0.1 mM, respectively

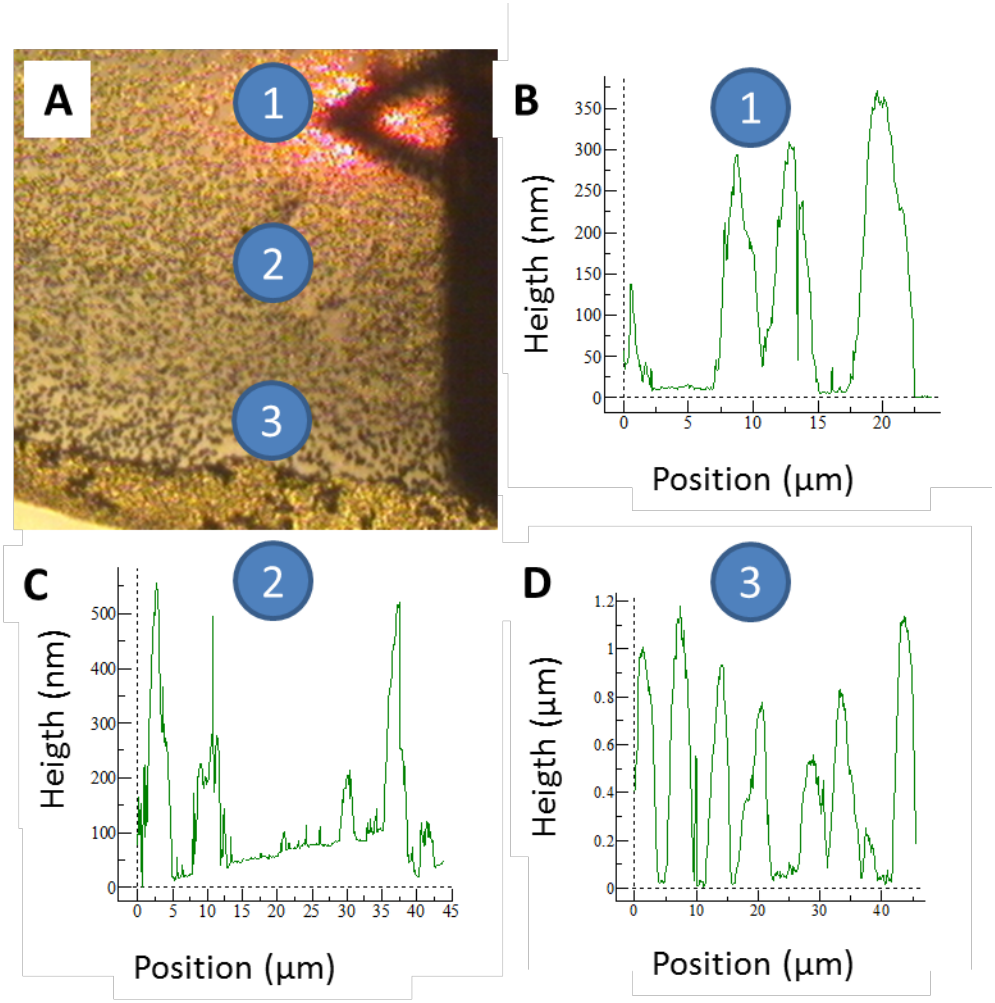

Figure S6. AFM characterization of MUDOL-GNR supercrystals with an Au^0 concentration before drop casting of 15 mM. **A)** Optical microscopy image showing approximately areas denoted 1, 2 and 3 where AFM mapping in B-D was performed-**B-D)** Height profile in AFM of supercrystals in region 1, 2 and 3. **B)** Close to the center of the drop, an average supercrystal height of 300 nm was measured. **C)** Closer to the coffee ring region, an average supercrystal height of 400 nm was measured. **D)** Very close to the coffee ring region, an average supercrystal height of 1 µm was measured. CTAB and MUDOL concentrations were below CMC and 0.1 mM, respectively.

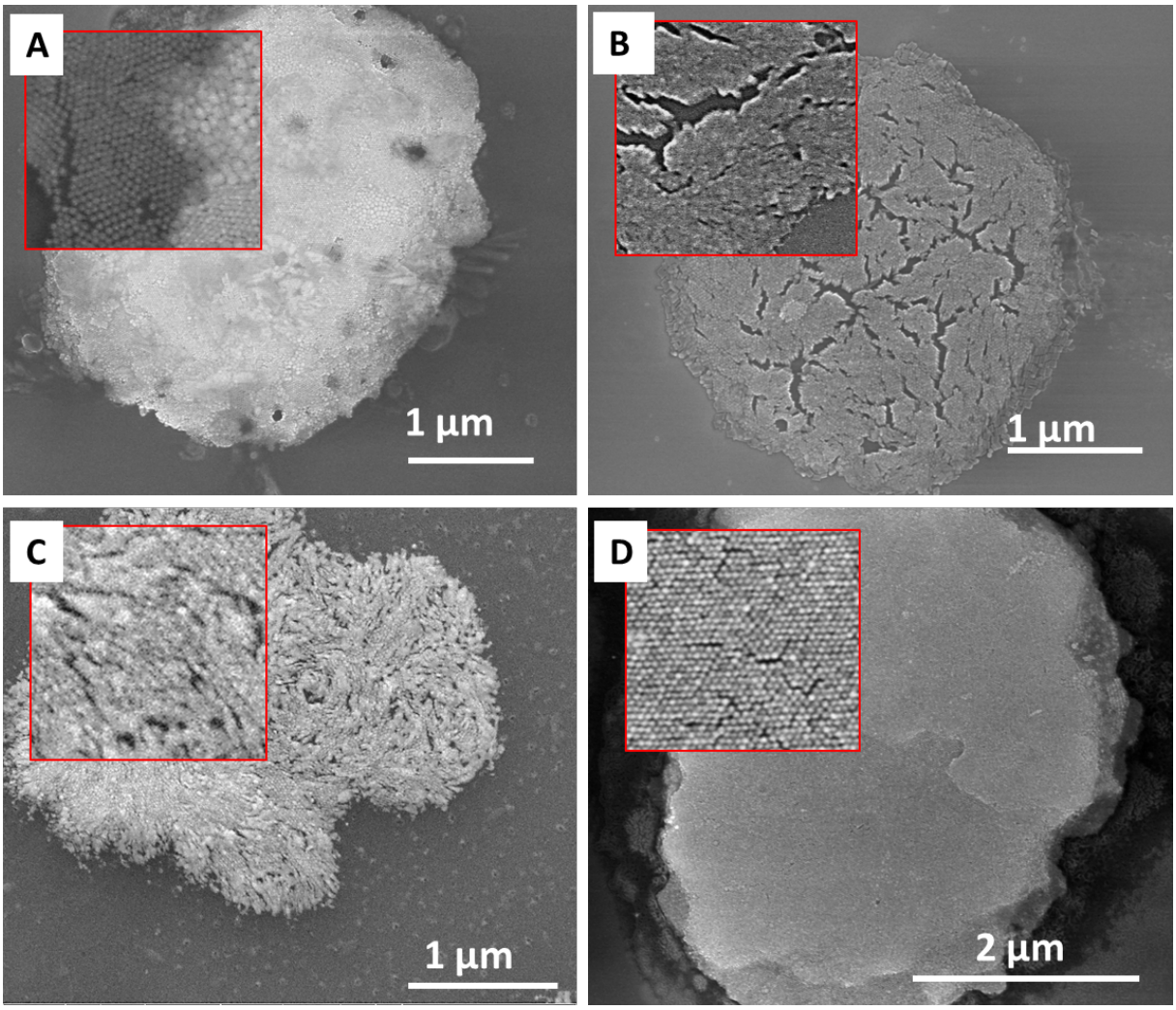

Figure S7. Comparison of cleaning processes to remove organics from the supercrystals surface, characterized by SEM. **A)** As prepared supercrystals. **B)** Supercrystals after one hour UV/O_3; formation of defects on the surface was observed as previously reported.[17] **C)** Supercrystals after O_2 plasma (200 W, 0.4 mbar O_2, 30 sec); a lot of defects and aggregates were found. **D)** Supercrystals after Ar cleaning (4W, 24 mbar Ar, 30 min).

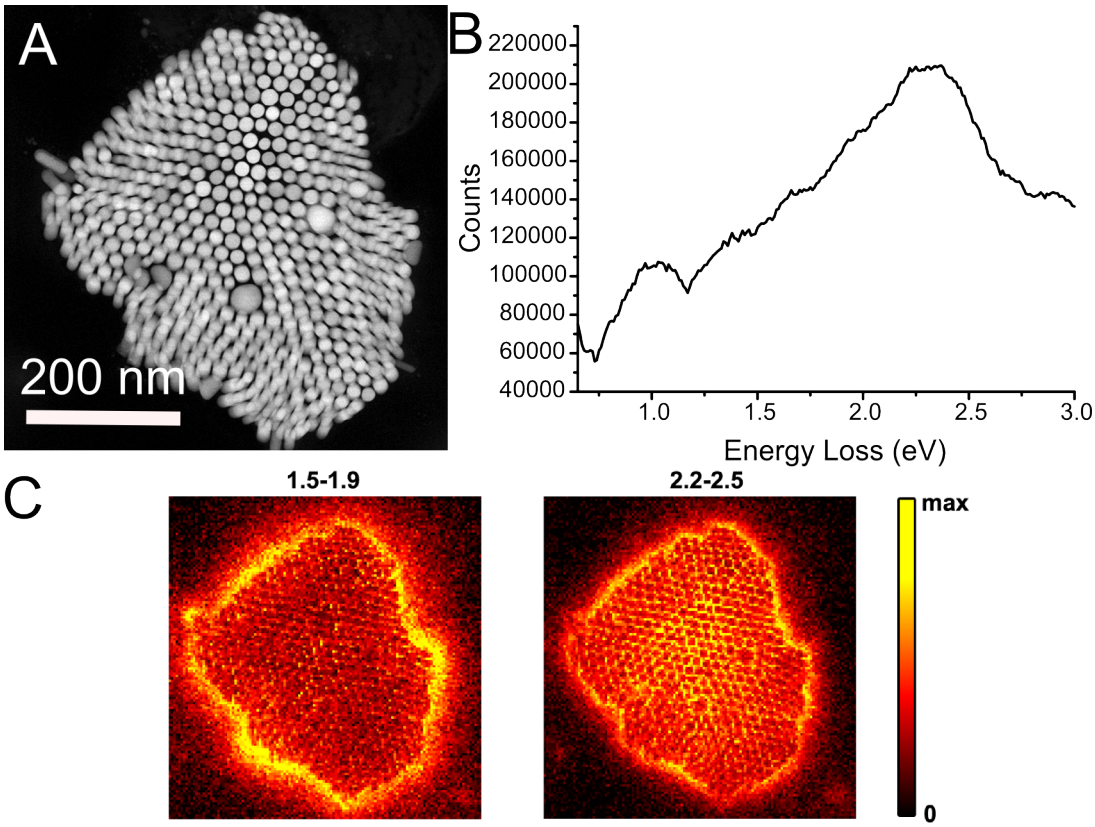

Figure S8. EELS plasmon mapping of a GNR monolayer. **A)** HAADF-STEM image of a GNR monolayer on a SiN film. **B)** EELS spectrum showing one strong peak at 2.1-2.5 eV and a shoulder at 1.5-1.9 eV. **C)** Plasmon maps showing the plasmon modes present in the spectrum presented in B.

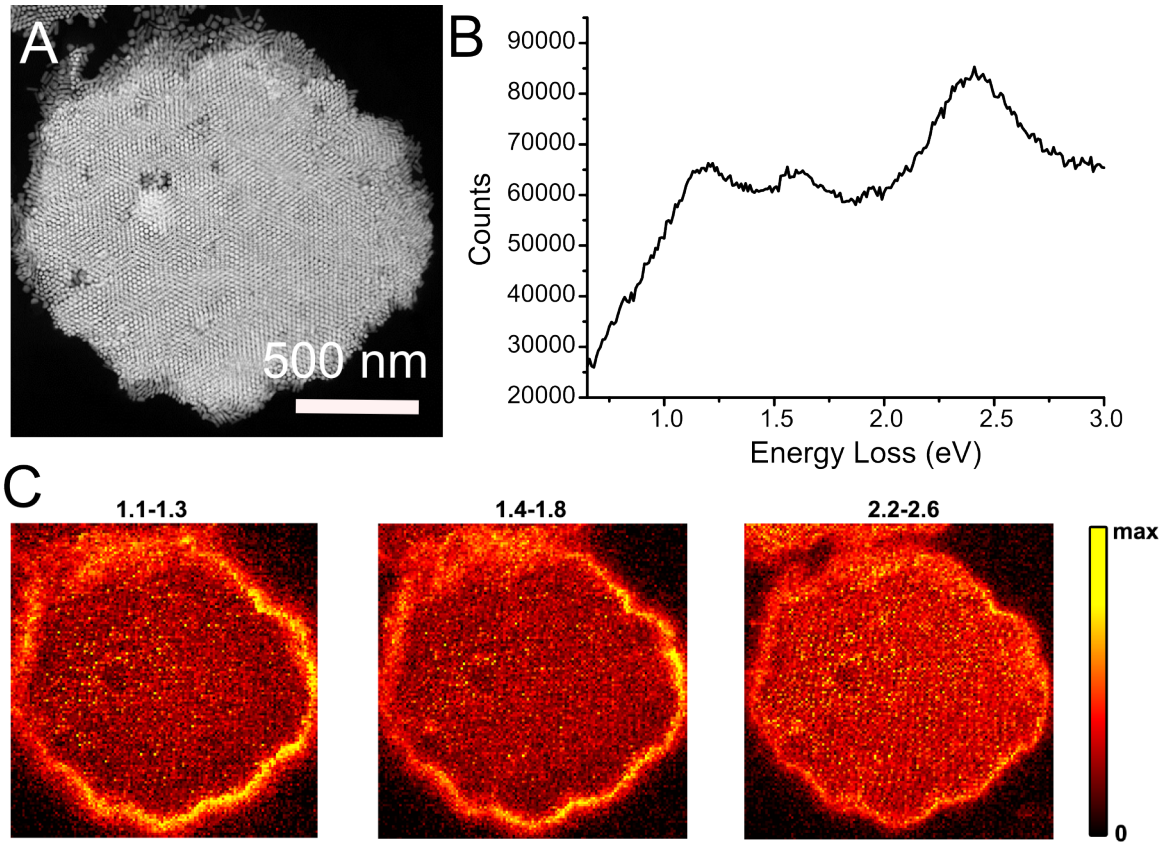

Figure S9. EELS plasmon mapping of a GNR bilayer. **A)** HAADF-STEM image of a bilayer assembly of Au NRs standing on a SiN film. **B)** EELS spectrum showing three peaks at 2.2-2.6 eV, 1.4-1.8 eV and 1.1-1.3 eV, respectively. **C)** Corresponding plasmon maps showing the different modes present in the spectrum presented in B.

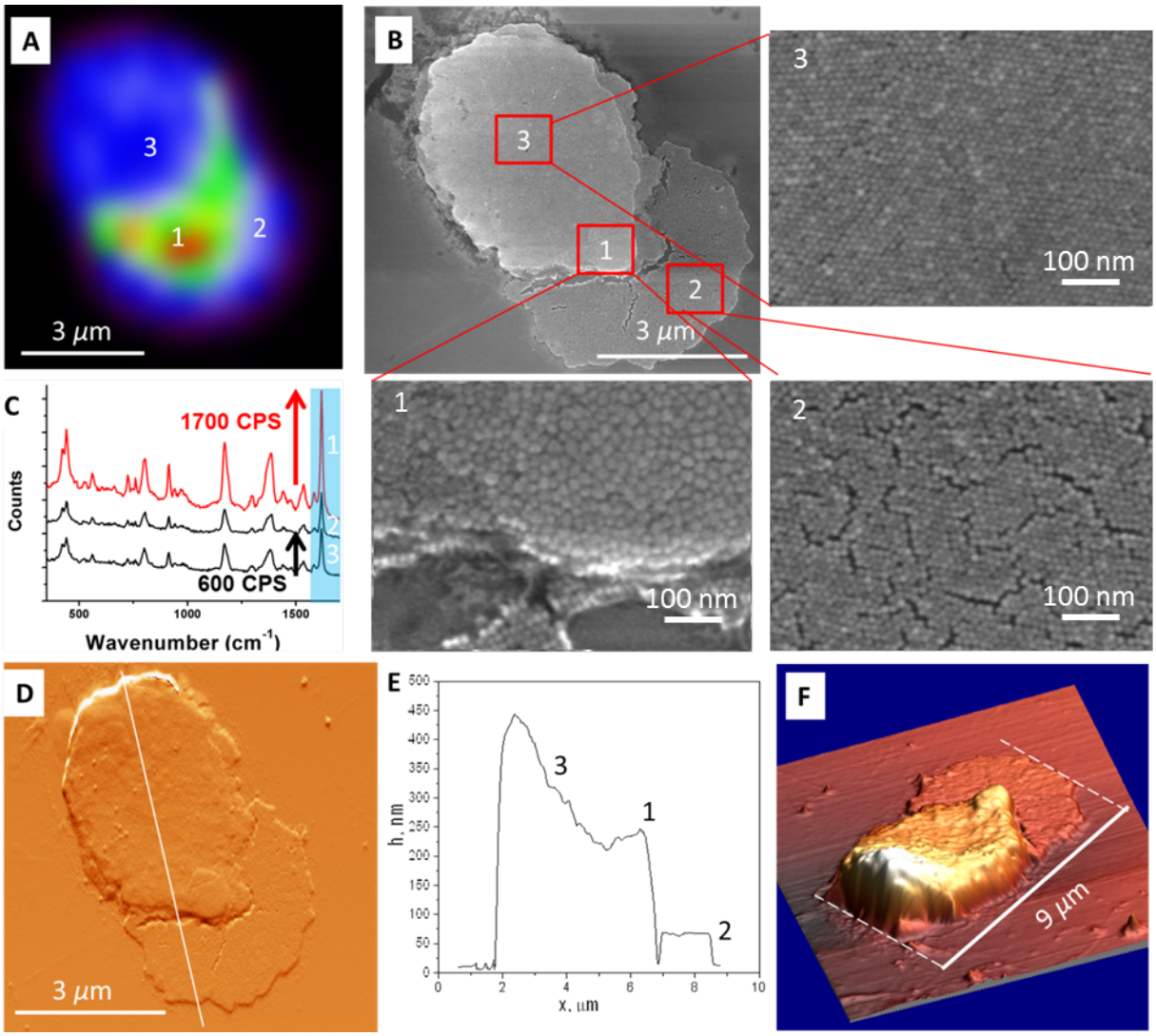

Figure S10. Characterization of GNR multilayers. All measurements were performed on the same supercystal. **A)** SERS image obtained by mapping SERS intensity of the crystal violet vibrational peak over 1618-1632 cm^{-1}. **B)** SEM images of the supercrystal at different magnifications, demonstrating organization at the surface in relevant areas **C)** Average SERS spectra of CV in the regions denoted as 1, 2, 3. Note that the signal intensity in region 2 (monolayer) is the same as in region 3 (multilayers). Region 1 showing surface defects yields a higher signal. CV concentration was 10^{-6} M in ethanol, drop-casted on the substrate and dried under ambient conditions. The acquisition time was 500 ms, and the laser power was ≈0.15mW at an excitation wavelength of 633 nm. **D)** AFM image of the supercrystal. **E)** Height profile along the white line shown in D). **F)** Three dimensional AFM topography plot of the supercrystal.

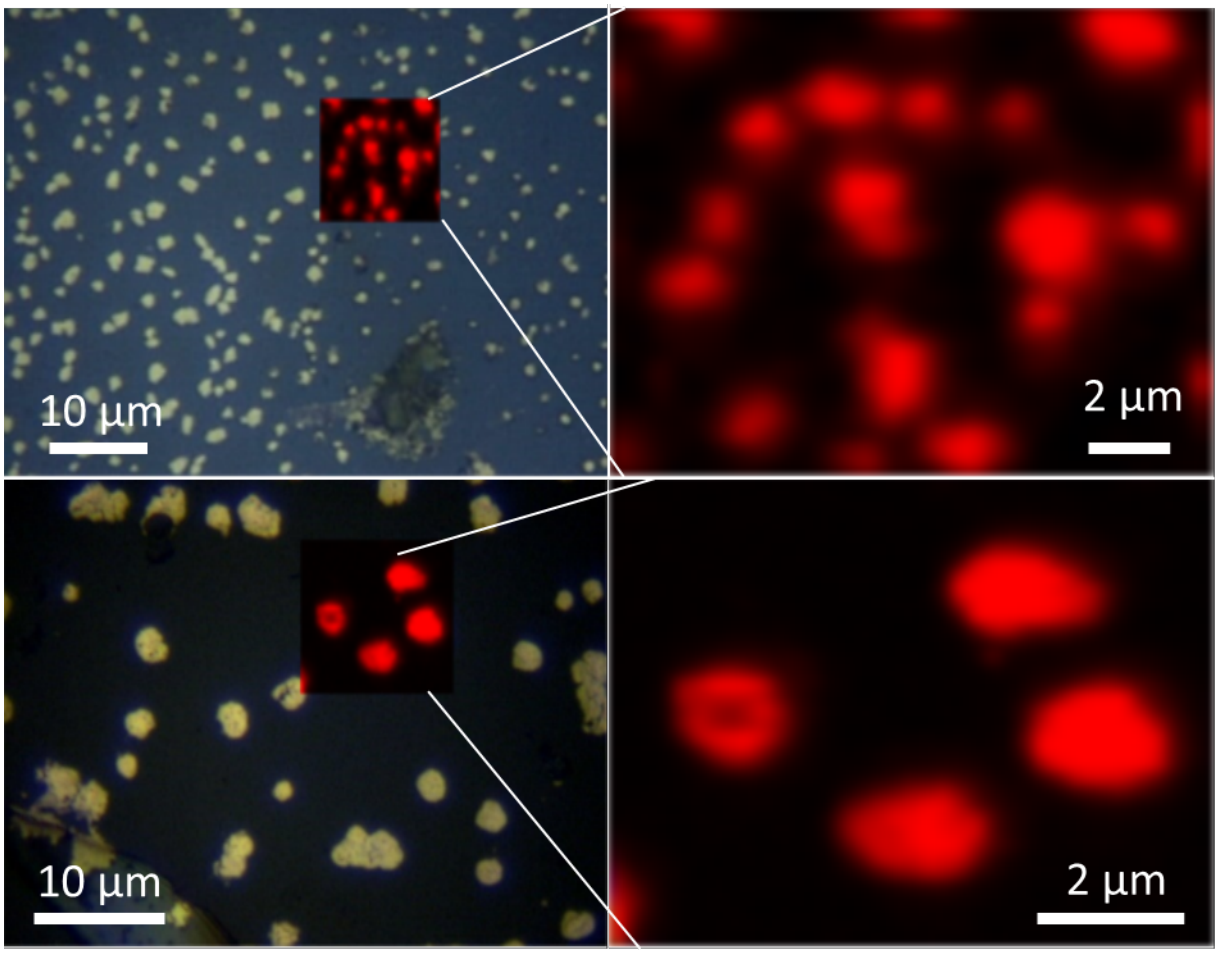

Figure S11. Large area Raman mappings on random supercrystals showing homogeneous signal intensity. Left panel: optical microscopy images of the samples where Raman scattering was measured. Right panel: SERS images obtained by mapping SERS intensity of the CV vibrational peak over 1618-1632 cm^{-1}. Concentration of CV before drop casting was 10^{-6} M, acquisition time 500 ms, and laser power ≈0.01 mW, at an excitation wavelength of 633 nm.

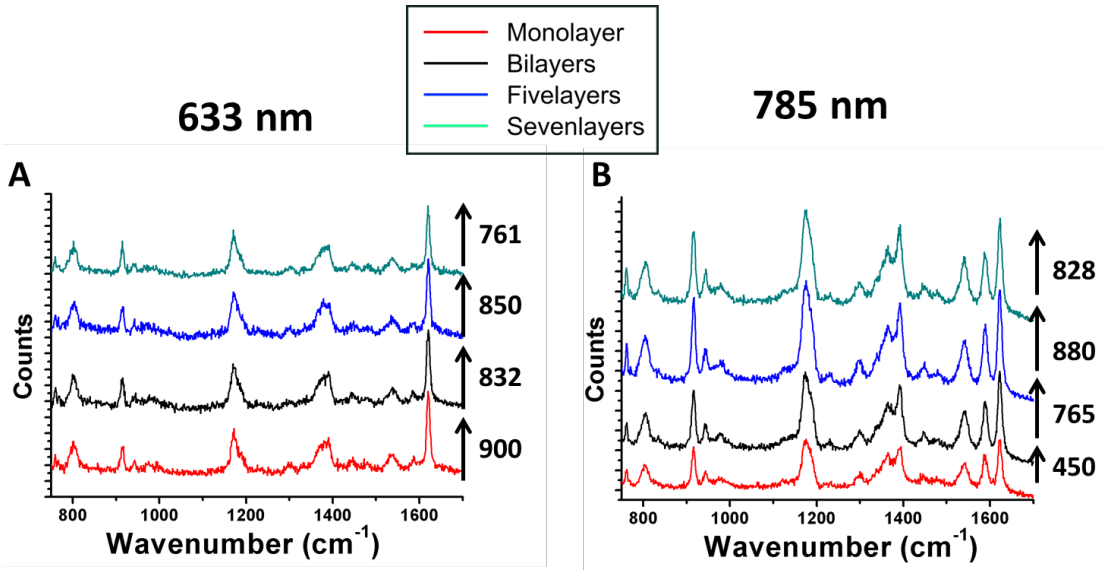

Figure S12. Comparison of SERS spectra of CV deposited on the surface of multilayers at 633 nm (A) and 785 nm (B). Laser power was 0.01 mW at 633 nm and 1.16 mW at 785 nm, all other parameters were fixed: CV concentration before drop casting 10^{-6} M and acquisition time 500 ms.

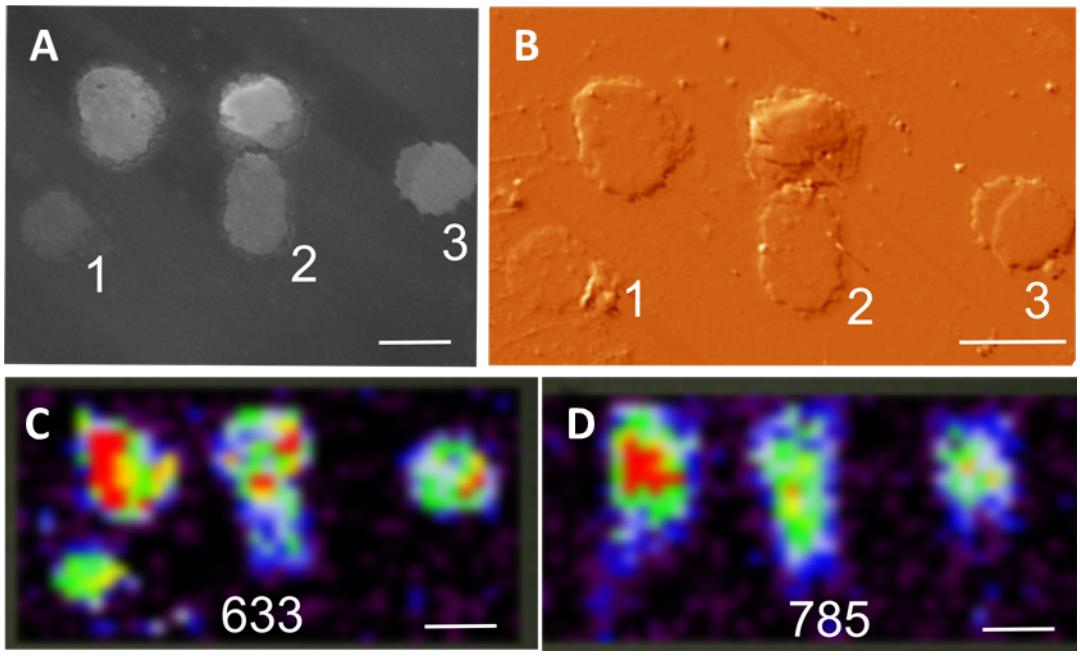

Figure S13. Comparison of CV SERS signal multilayers. A,B) SEM image of GNR supercrystals indicating number of layers. C,D) SERS images of the same area acquired with excitation wavelengths of 633 nm (C) and 785 nm (D). The monolayer is not visible in D. SERS images were obtained by mapping SERS intensity of CV vibrational peak over 1618-1632 cm^{-1}. Laser power was 0.01 mW at 633 nm and 1.16 mW at 785 nm, all other parameters were fixed: CV concentration before drop casting 10^{-6} M and acquisition time 500 ms.

References

(1) Verbeeck, J.; Van Aert, S. *Ultramicroscopy* **2004**, *101*, 207-224.

(2) Verbeeck, J. & van Aert, S., Available at www.eelsmodel.uantwerpen.be

(3) J. R. Kremer, D. N. *J. Struct. Biol.* **1996**, *116*, 71-76.

(4) W., Van Aarle, Palenstijn W.J., De Beenhouwer J., Altantzis T., Bals S., Batenburg K.J., S. J. *Ultramicroscopy* **2015**, *157*, 35–47.

(5) Palenstijn, W. J.; Batenburg, K. J.; Sijbers, *J. Struct. Biol.* **2011**, *176*, 250-253.

(6) Scarabelli, L.; Grzelczak, M.; Liz-Marzán, L. M. *Chem. Mater.* **2013**, *25*, 4232–4238.

(7) Hamon, C.; Novikov, S.; Scarabelli, L.; Basabe-Desmonts, L.; Liz-Marzán, L. M. *ACS Nano* **2014**, *8*, 10694-10703.

(8) Solís, D. M.; Taboada, J. M.; Obelleiro, F. *IEEE Trans. Antennas Propag.* **2015**, *63*, 2141-2152

(9) Rao, S. M.; Wilton, D.; Glisson, A. W. *IEEE Trans. Antennas Propag.* **1982**, *30*, 409-418.

(10) Coifman, R.; Rokhlin, V.; Wandzura, S. *IEEE Antennas Propag. Mag.* **1993**, *35*, 7-12.

(11) Jiming, S.; Cai-Cheng, L.; Weng Cho, C. *IEEE Antennas Propag. Mag.* **1997**, *45*, 1488-1493.

(12) Taboada, J. M.; Araújo, M. G.; Obelleiro, F.; Rodríguez, J. L.; Landesa, L. *Proc. IEEE* **2013**, *101*, 350-363.

(13) Solís, D. M.; Taboada, J. M.; Obelleiro, F.; Liz-Marzán, L. M.; García de Abajo, F. J. *ACS Nano* **2014**, *8*, 7559–7570.

(14) Solis, D. M.; Araujo, M. G.; Landesa, L.; Garcia, S.; Taboada, J. M.; Obelleiro, F. *IEEE Photon. J.* **2015**, *7*, 1-9.

(15) Loan, G. H. G. a. C. F. V. *Matrix Computations.* **1989**.

(16) Johnson, P. B.; Christy, R. W. *Phys. Rev. B* **1972**, *6*, 4370-4379.

(17) Peng, B.; Li, G.; Li, D.; Dodson, S.; Zhang, Q.; Zhang, J.; Lee, Y. H.; Demir, H. V.; Ling, X. Y.; Xiong, Q. *ACS Nano* **2013**, *7*,5993–6000.